Electronic Supplementary Material (ESI) for Energy & Environmental Science.

Surface ions-activated polymer composites dielectrics for superior high-temperature capacitive energy storage

Minhao Yang[1, 2 *]*, Yanlong Zhao*[1, 2]*, Zepeng Wang*[1, 2]*, Huarui Yan*[1, 2]*, Zeren Liu*[1, 2]*, Qi. Li*[3, *]*, Zhi-Min Dang*[3, *]

[1] *Institute of Energy Power Innovation, North China Electric Power University, Beijing, 102206, China*

[2] *State Key Laboratory of Alternate Electrical Power System with Renewable Energy Sources, North China Electric Power University, Beijing, 102206, China*

[3] *State Key Laboratory of Power System Operation and Control, Department of Electrical Engineering, Tsinghua University, Beijing, 100084, China*

Corresponding Authors: minhao.yang@ncepu.edu.cn; qili1020@mail.tsinghua.edu.cn; dangzm@tsinghua.edu.cn

1. Dielectric breakdown stength measurements:

Breakdown strength results are analyzed using two-parameter Weibull statistic described as

$$P(E) = 1 - exp(- (E/\alpha)^{\beta})$$

Where $P(E)$ represents the cumulative probability of breakdown failure, E denotes the experimental electric field, α is the scale parameter, which is the breakdown strength at cumulative failure probability of 63.2%. The shape parameter β is the slope of the fitted Weibull curve, suggesting the scattering of the experiment results.

2. Conduction mechanism:

(1) Conduction in the lower electric field range:

Schottky emission is the main mechanism for the electrode-limited conduction loss in the lower electric field regime at elevated temperatures. The thermally activated electrons from the electrode can overcome the energy barrier height at the interface of the electrode and dielectric, followed by being injected into the dielectric surface. The Schottky emission model related to the leakage current density (J) and electric field (E) can be expressed by[3]

$$J = AT^2 exp(\frac{- q(\varphi - \sqrt{qE/4\pi\varepsilon_i\varepsilon_0})}{kT})$$

where A denotes Richardson constant, T is the absolute temperature, q is the electronic charge, $q\phi$ represents the barrier height, k is Boltzmann's constant, ε_0 is the vacuum dielectric constant, and ε_i is the optical dielectric constant. The $\ln J$ is linearly proportional to $\sqrt{E}$. The calculated injection barrier height for PEI, H-PEI, Al_2O_3/PEI and H-Al_2O_3/PEI films are 1.071 eV, 1.127 eV, 1.135 eV and 1.151 eV, respectively.

(2) Conduction in the higher electric field range:

The hopping conduction is the main mechanism for the bulk-limited conduction loss in the higher electric field range at high temperatures. The hopping conduction describes the transport of carriers inside the bulk phase of dielectrics.[3] The thermally activated carriers can leave their localized state and move to another localized state.

$$J = 2qdnv \times exp(-\frac{E_a}{kT}) \times sinh(\frac{qdE}{2kT})$$

Where d is the average hopping distance between adjacent trap centers, n is the electron concentration in the dielectric, v is the thermal vibration frequency of trapped electrons, and E_α is the activation energy, E is the electric field, q is the electron charge, k is Boltzmann constant and T is the temperature, respectively. A smaller hopping distance usually represents the increase in trap density. The calculated hopping distance for PEI, H-PEI, Al_2O_3/PEI and H-Al_2O_3/PEI films are 0.81 nm, 0.79 nm, 0.74 nm and 0.66 nm, respectively.

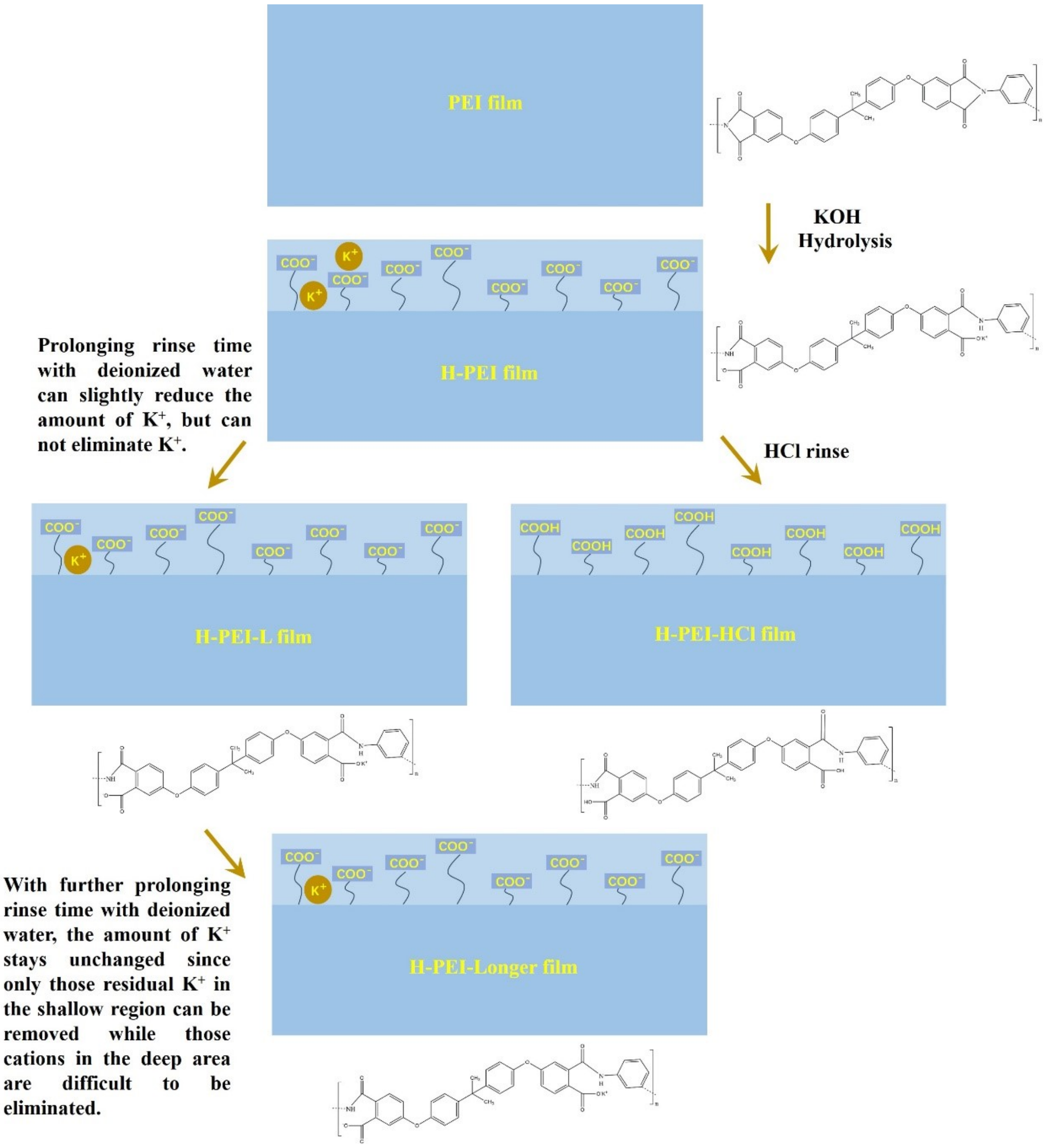

Prolonging rinse time with deionized water can slightly reduce the amount of K^+, but can not eliminate K^+.

With further prolonging rinse time with deionized water, the amount of K^+ stays unchanged since only those residual K^+ in the shallow region can be removed while those cations in the deep area are difficult to be eliminated.

Figure S1. Schematic illustrating the hydrolysis and rinse processes of PEI films.

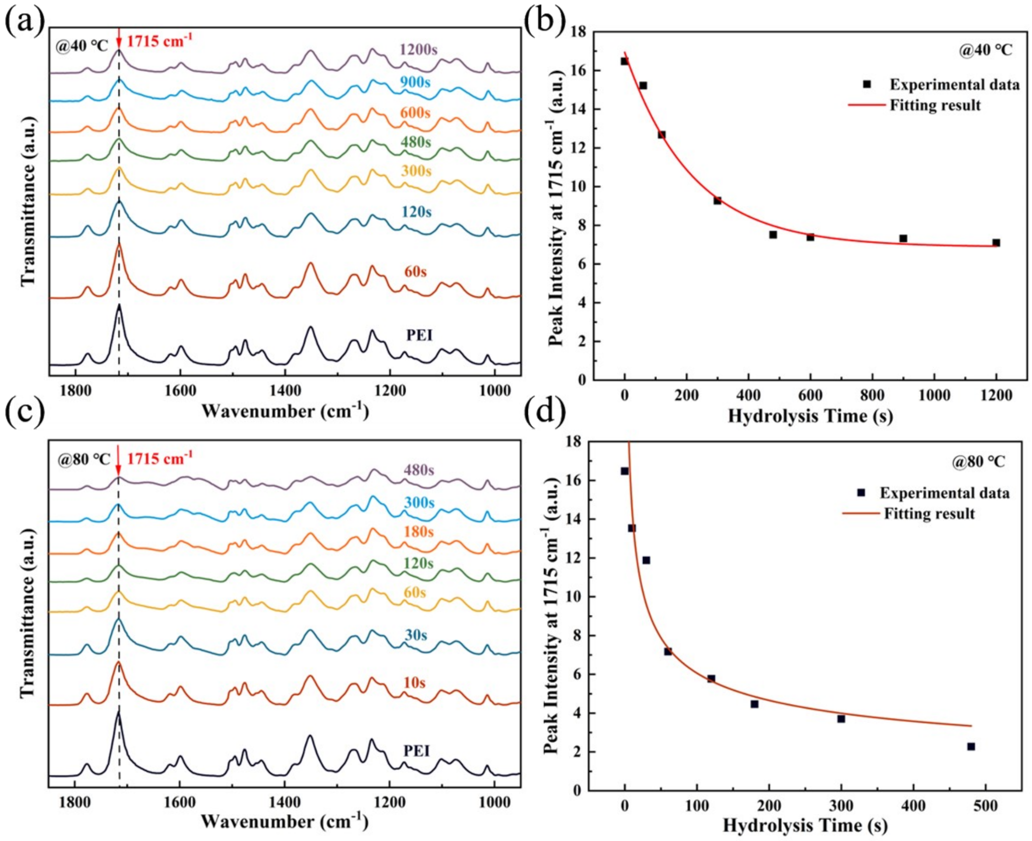

Figure S2. (a) FT-IR spectra of pristine PEI and H-PEI with various hydrolysis periods at 40 ℃. (b) The hydrolytic degree of PEI films as a function of hydrolysis period at 40 ℃. (c) FT-IR spectra of pristine PEI and H-PEI with various hydrolysis periods at 80 ℃. (d) The hydrolytic degree of PEI films as a function of hydrolysis period at 80 ℃.

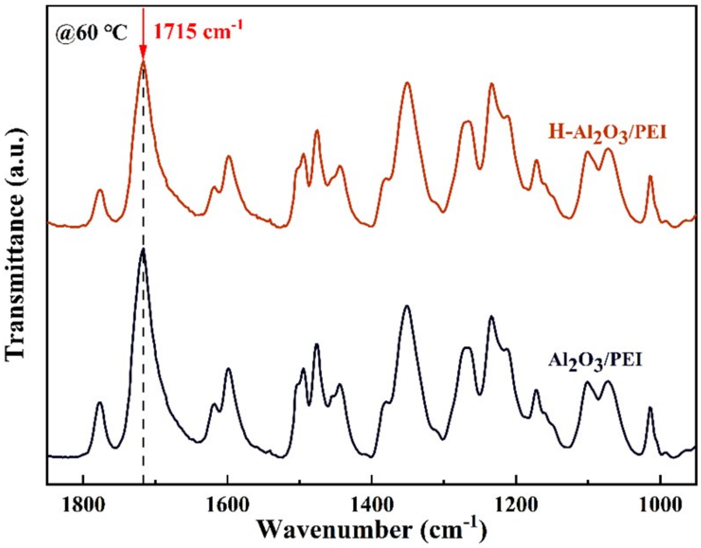

Figure S3. Comparison of FT-IR spectra of Al_2O_3/PEI and H-Al_2O_3/PEI films.

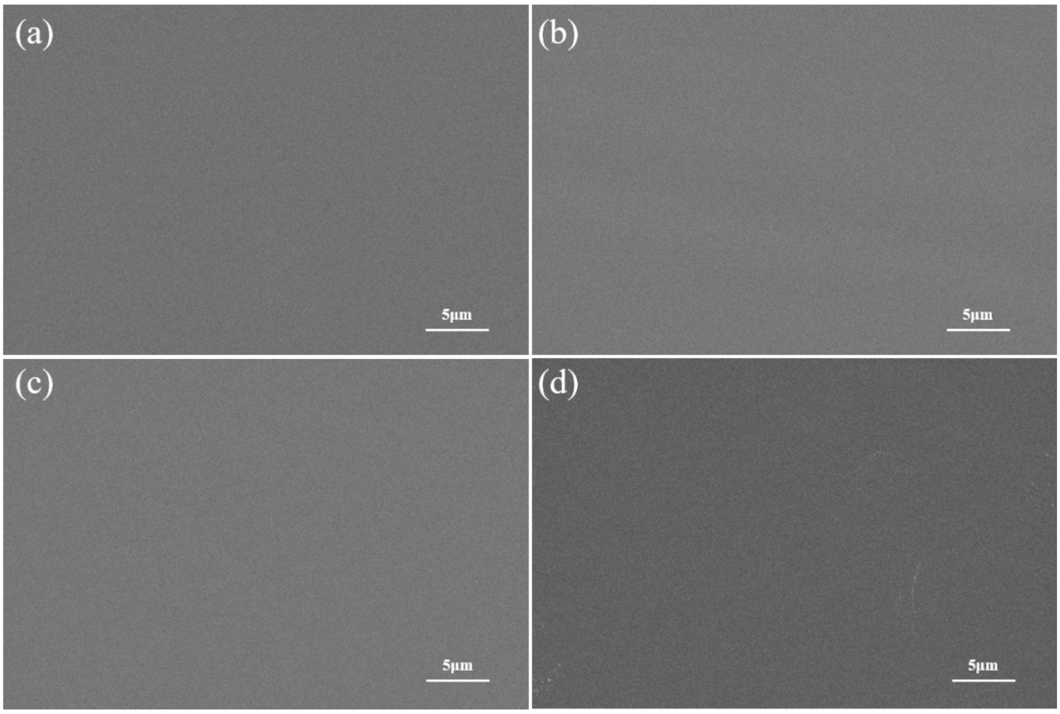

Figure S4. SEM images of the surface morphologies of (a) pristine PEI, (b) H_{30s}-PEI, (c) H_{120s}-PEI and (d) H_{480s}-PEI films.

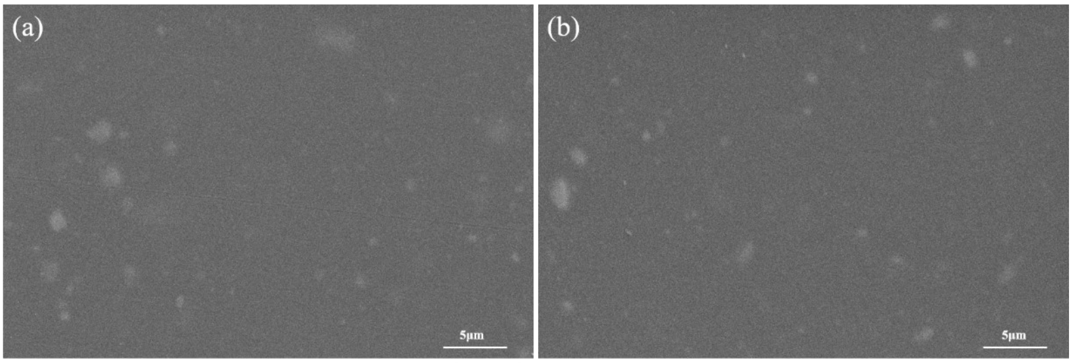

Figure S5. SEM images of the surface morphologies of (a) Al_2O_3/PEI and (b) H-Al_2O_3/PEI films.

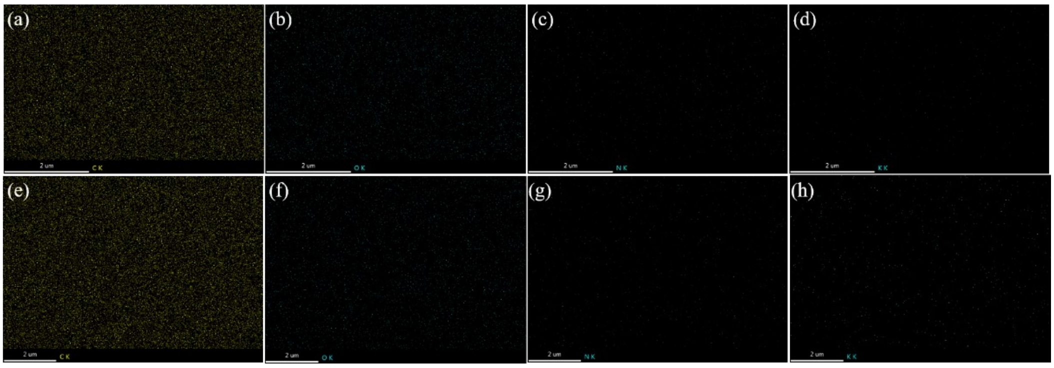

Figure S6. EDS spectrum of (a-d) pristine PEI and (e-h) H_{480s}-PEI films with C, O, N and K elements.

Table S1. Binding energies of elements of the PEI and H-EPI films.

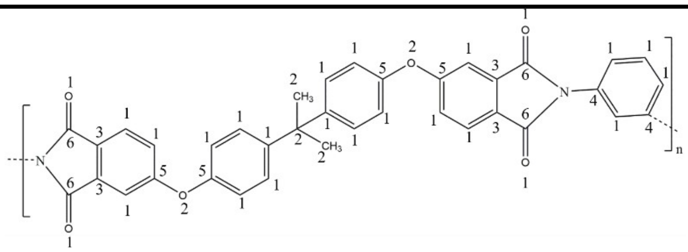

Atomic	C_{1s}			O_{1s}		N_{1s}	K_{2p}	
element	C-1	C-2	C-3	O-1	O-2		K-1	K-2
	1 2 3	4 5	6	1	2			
BE (eV)	284.6	286.2	288.3	531.7	533.2	400.3	292.9	295.6

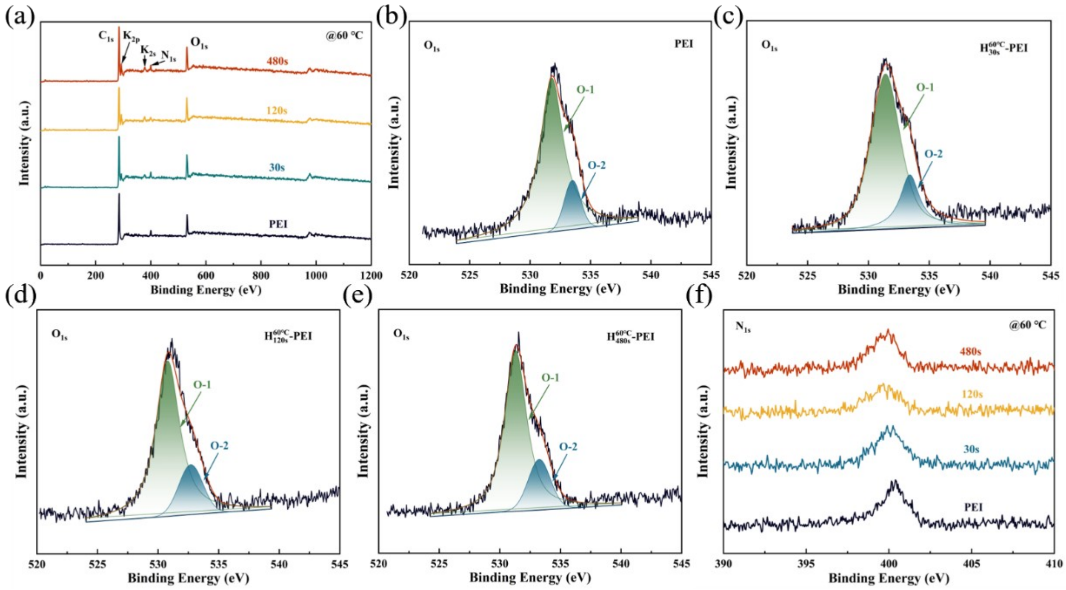

Figure S7. (a) XPS survey spectrum of pristine PEI and H-PEI films with various hydrolysis time. XPS O_{1s} spectrum of (b) pristine PEI and (c-e) H-PEI films with various hydrolysis time. (f) XPS N_{1s} spectrum of PEI and H-PEI films with various hydrolysis time.

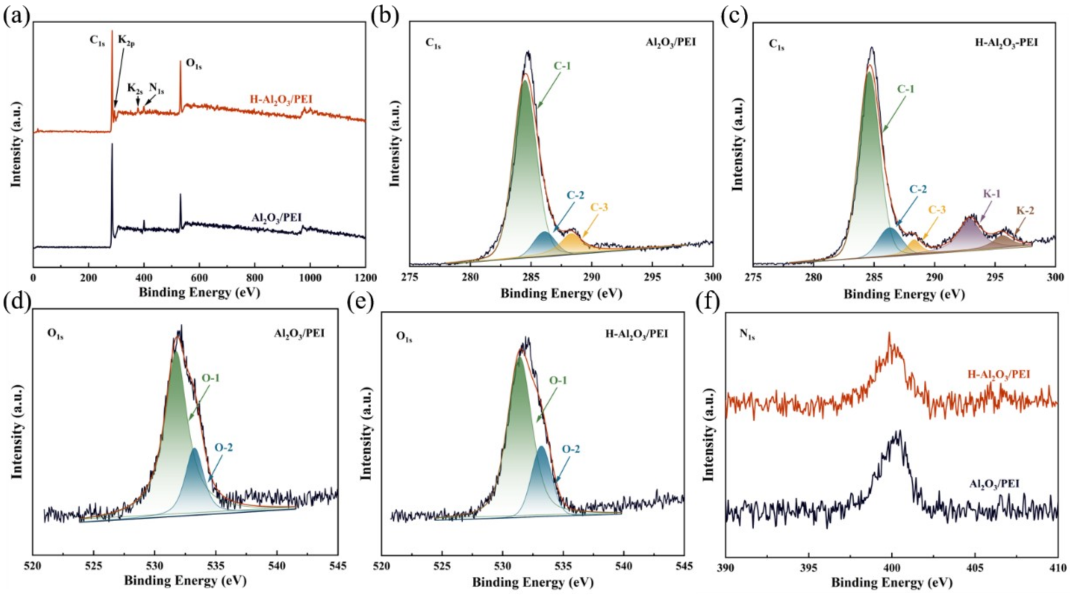

Figure S8. (a) XPS survey spectrum of Al_2O_3/PEI and H-Al_2O_3/PEI films. XPS C_{1s} spectrum of (b) Al_2O_3/PEI and (c) H-Al_2O_3/PEI films. XPS O_{1s} spectrum of (d) Al_2O_3/PEI and (e) H-Al_2O_3/PEI films. (f) XPS N_{1s} spectrum of Al_2O_3/PEI and H-Al_2O_3/PEI films.

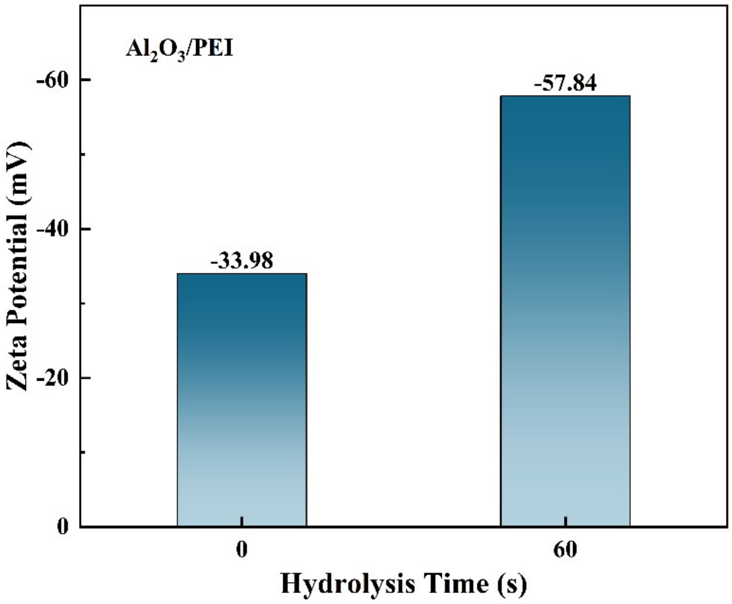

Figure S9. Zeta potential of Al_2O_3/PEI and H-Al_2O_3/PEI films.

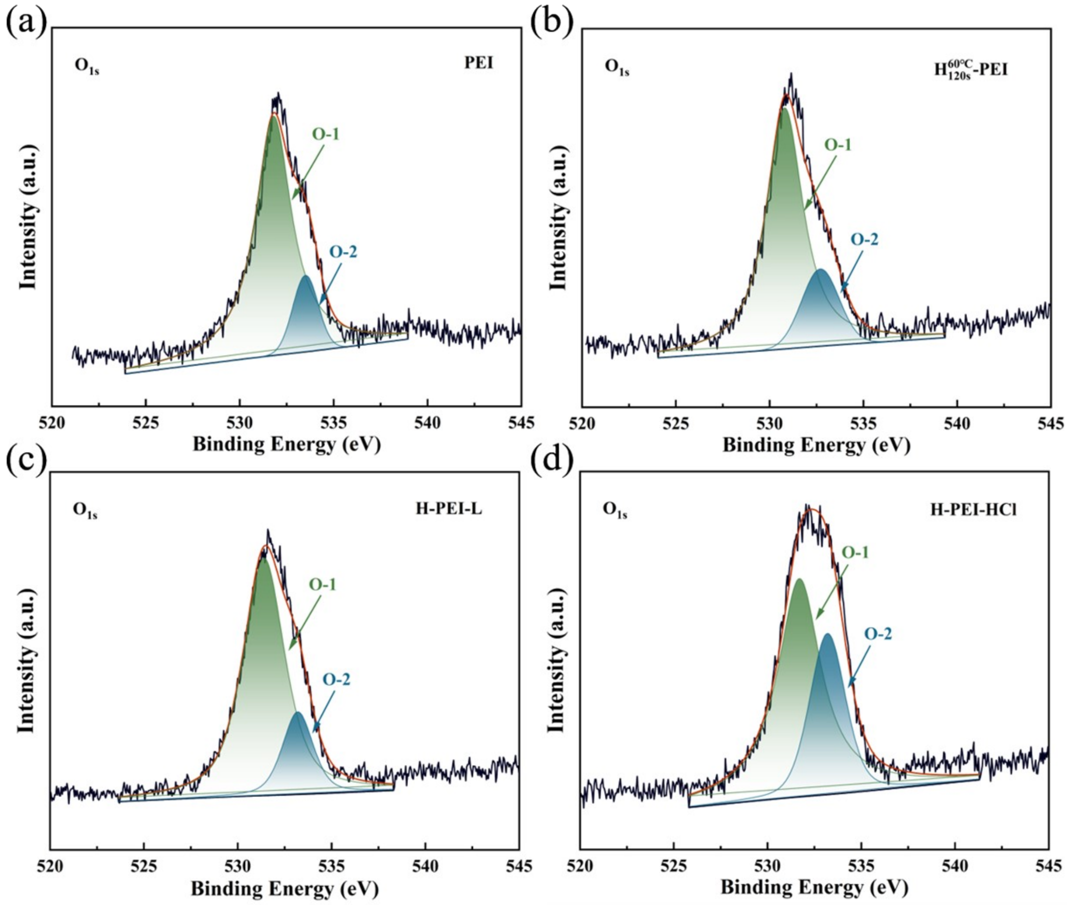

Figure S10. XPS O_{1s} spectrum of (a) pristine PEI, (b) H-PEI, (c) H-PEI-L and (d) H-PEI-HCl films.

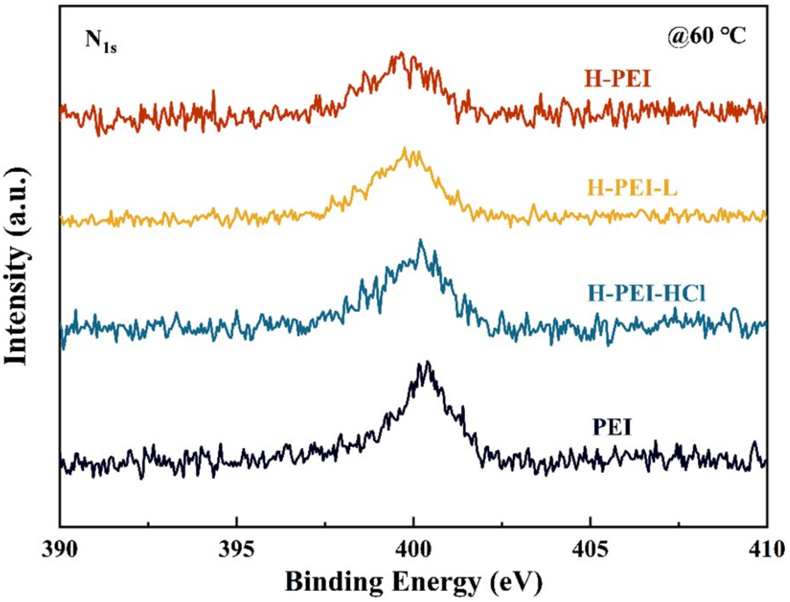

Figure S11. XPS N_{1s} spectrum of pristine PEI, H-PEI, H-PEI-L and H-PEI-HCl films.

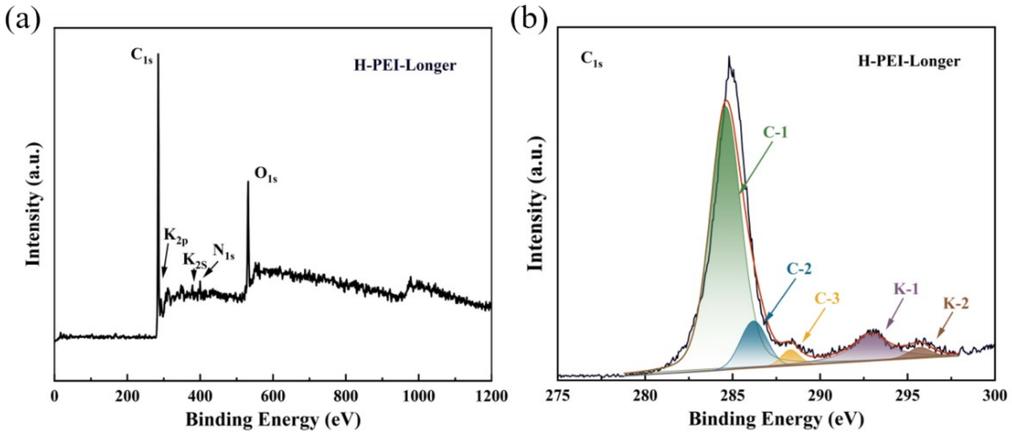

Figure S12. (a) XPS survey and (b) C_{1s} spectrum of H-PEI-Longer film.

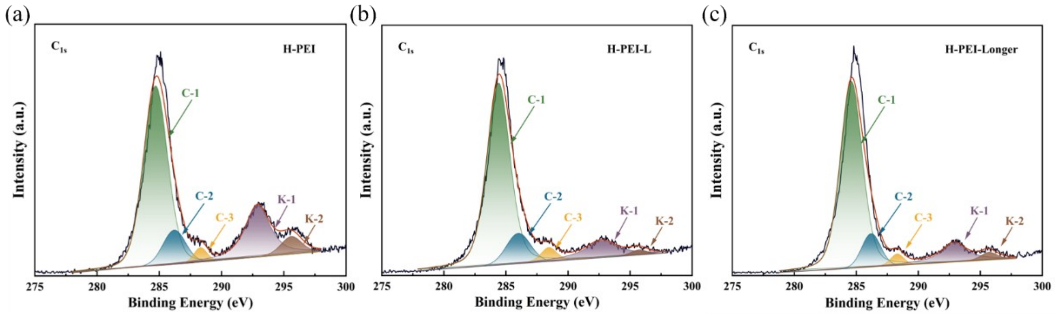

Figure S13. The comparison of XPS C_{1s} spectrum of H-PEI, H-PEI-L and H-PEI-Longer films.

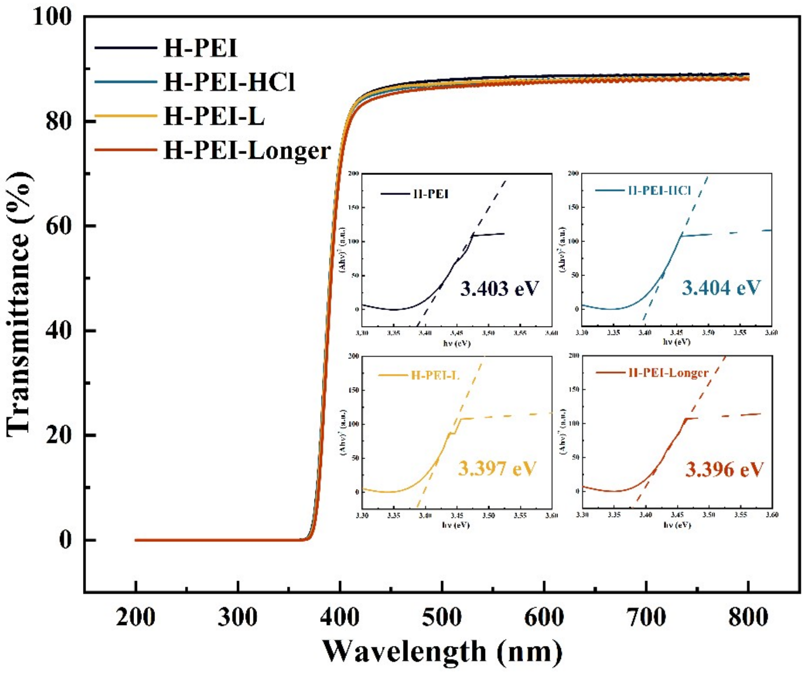

Figure S14. UV-vis spectrum of pristine PEI, H-PEI-HCl, H-PEI-L and H-PEI-Longer films, in which the inset exhibits the optical bandgaps calculated from the UV-vis spectrum.

Table S2. Statistical data of C_{1s}, O_{1s}, N_{1s}, K_{2s}, K_{2p} and Al_{2p} atomic percentages of PEI, H-PEI, Al_2O_3/PEI and H-Al_2O_3/PEI films from XPS survey.

Element categories	PEI Atom (%)	$H_{30s}^{60℃}$-PEI Atom (%)	$H_{120s}^{60℃}$-PEI Atom (%)	$H_{480s}^{60℃}$-PEI Atom (%)	$H_{120s}^{60℃}$-PEI-HCl Atom (%)	$H_{120s}^{60℃}$-PEI-L Atom (%)	Al_2O_3/PEI Atom (%)	H- Al_2O_3/PEI Atom (%)
C_{1s}	77.73	74.63	68.42	72.01	75.89	68.61	78.92	72.45
O_{1s}	15.45	16.76	18.64	18.4	17.07	21.62	14.47	17.83
N_{1s}	6.82	5.98	7.57	4.57	7.04	7.73	5.99	6.66
K_{2s}	0	0.36	0.93	0.85	0	0	0	0.63
K_{2p}	0	2.27	4.44	4.17	0	2.04	0	2.04
Al_{2p}	0	0	0	0	0	0	0.62	0.39

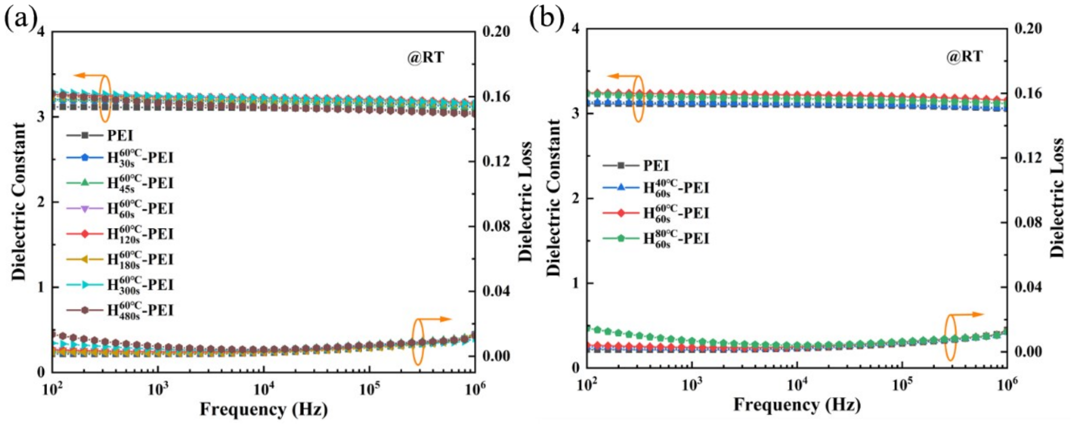

Figure S15. Frequency-dependent of the dielectric constant and dielectric loss of pristine PEI and H-PEI films with different hydrolysis (a) time (b) temperatures at room temperature.

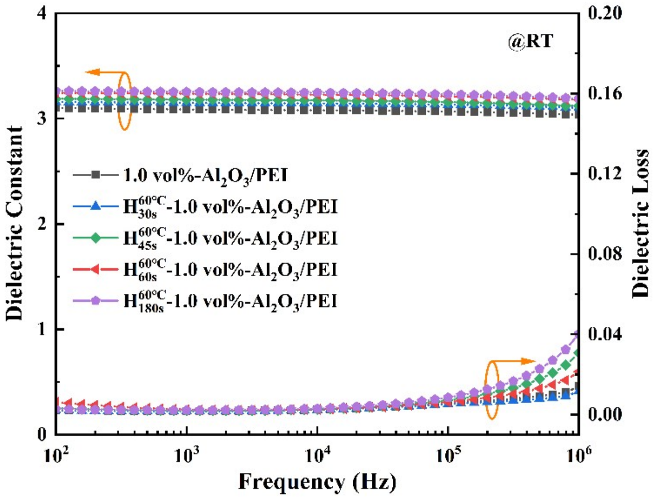

Figure S16. Frequency-dependent of the dielectric constant and dielectric loss of Al_2O_3/PEI and H-Al_2O_3/PEI films with different hydrolysis time at room temperature.

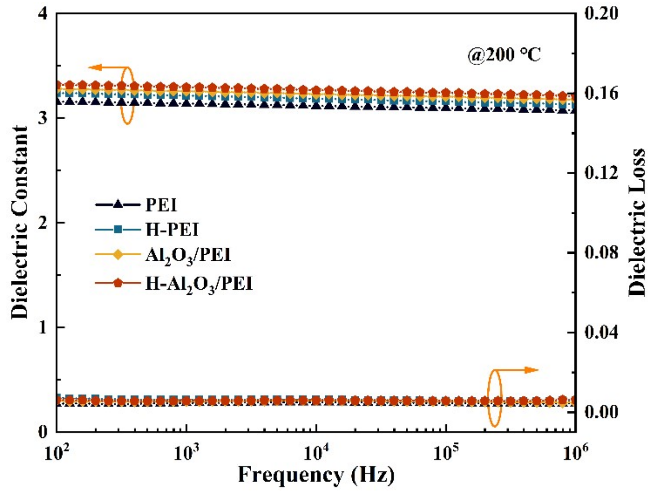

Figure S17. Frequency-dependent of the dielectric constant and dielectric loss of PEI, H-PEI, Al_2O_3/PEI and H-Al_2O_3/PEI films at 200 °C.

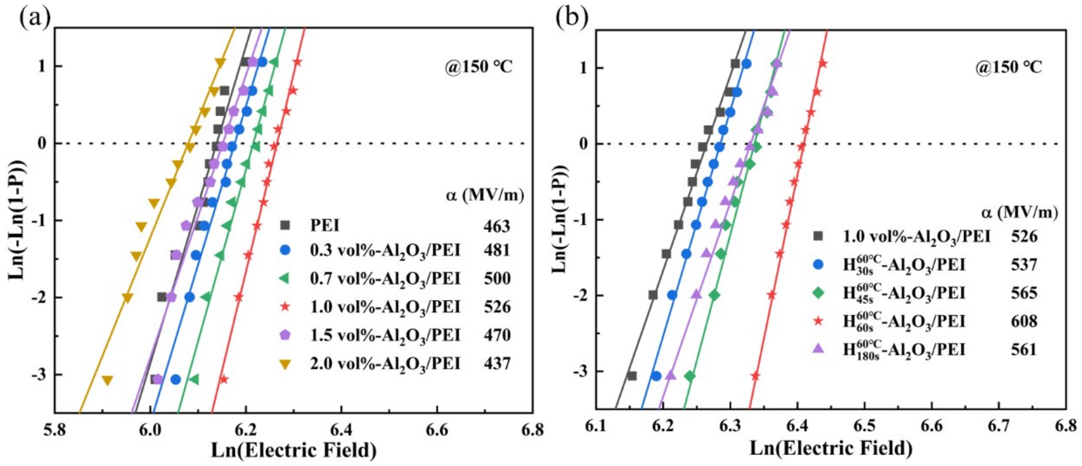

Figure S18. Weibull distribution analysis of (a) pristine PEI and Al_2O_3/PEI films with different loadings of Al_2O_3 at 150 ℃ and (b) H-Al_2O_3/PEI films with different hydrolysis time.

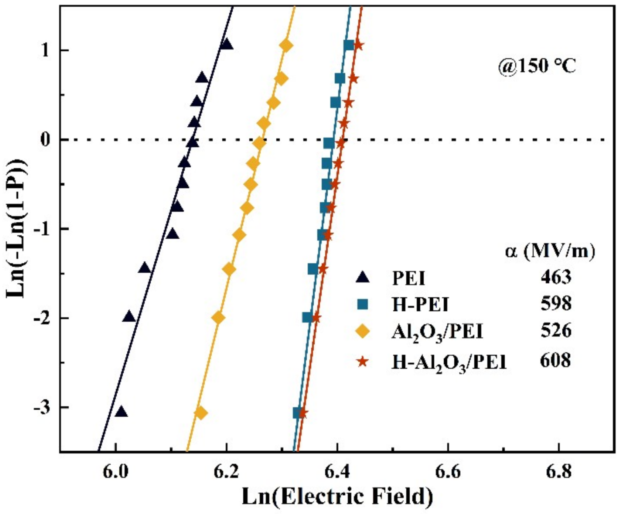

Figure S19. Weibull distribution analysis of PEI, H-PEI, Al_2O_3/PEI and H-Al_2O_3/PEI films at 150 ℃.

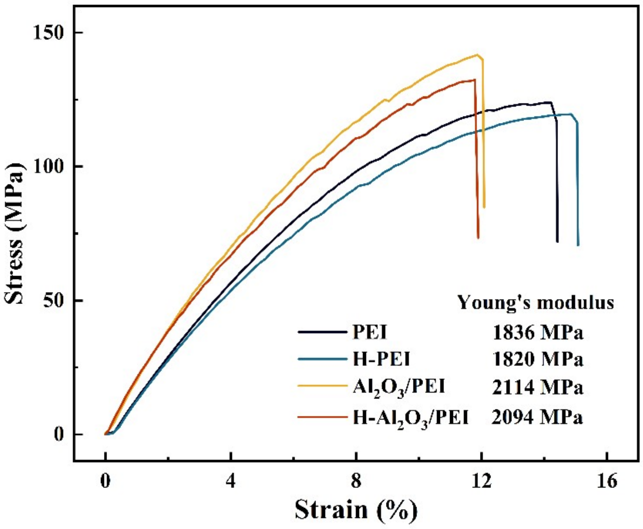

Figure S20. Stress-strain curves of PEI, H-PEI, Al_2O_3/PEI and H-Al_2O_3/PEI films.

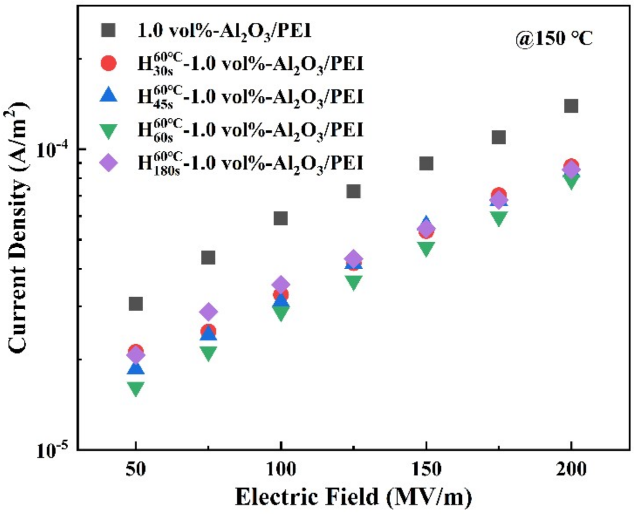

Figure S21. Leakage current density of H-Al_2O_3 and H-Al_2O_3/PEI films with different hydrolysis time.

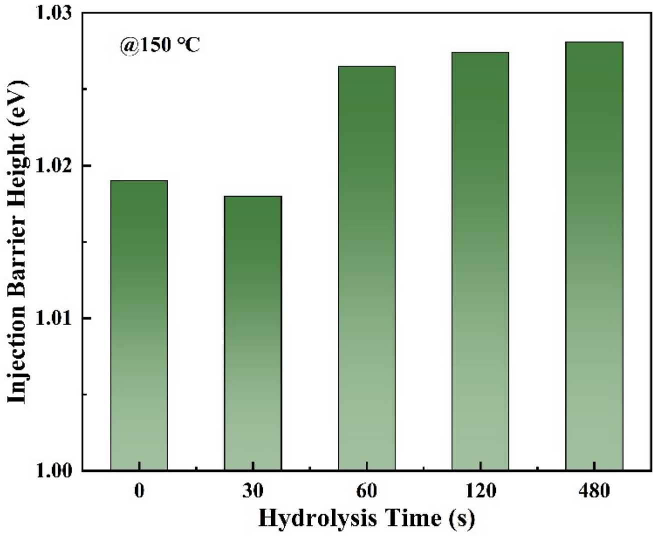

Figure S22. Comparison of calculated barrier height for the pristine PEI and H-PEI films with different hydrolysis time.

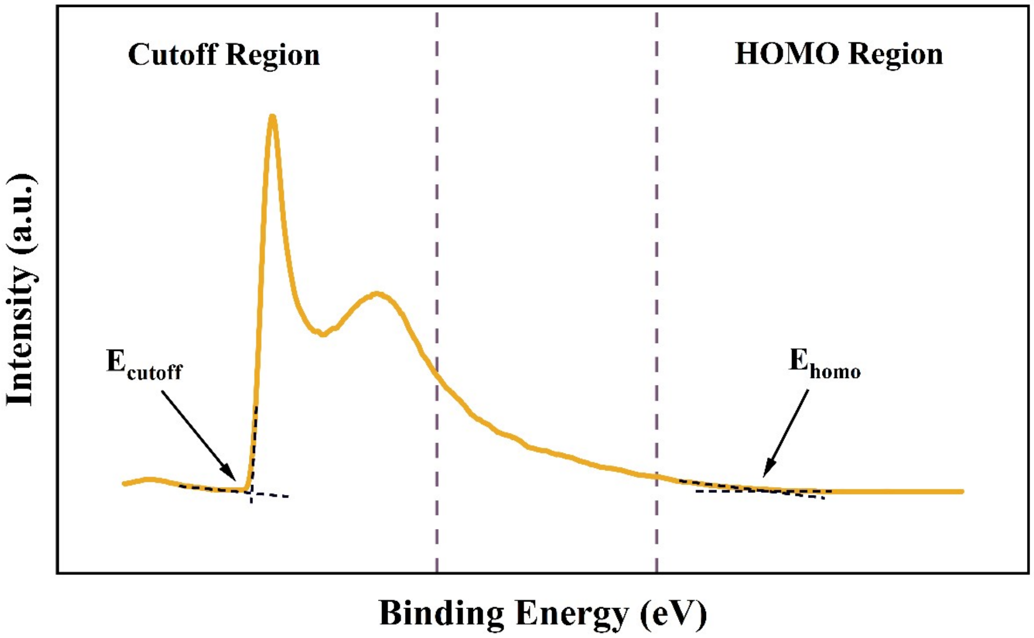

Figure S23. Schematic illustration of the ultraviolet photoelectron spectrum (UPS) for a polymer dielectric. In the UPS characterization, the electrons in the occupied state are excited by the incident photon energy (hν =21.22 eV). The work function (ϕ_p) is calculated by the difference between the photoelectron energy and the energy of secondary electron cutoff (E_{cutoff}).[1-2] The position of E_{cutoff} can be obtained from the intersection of the baseline and the tangents of the curve in the secondary electron cutoff region. E_{homo} is the minimum binding energy of photoelectron from the polymer dielectric (HOMO represents the highest occupied molecular orbital of the polymer dielectric). The position of E_{homo} can be extracted from the intersection of the baseline and the tangents of the curve in HOMO region.

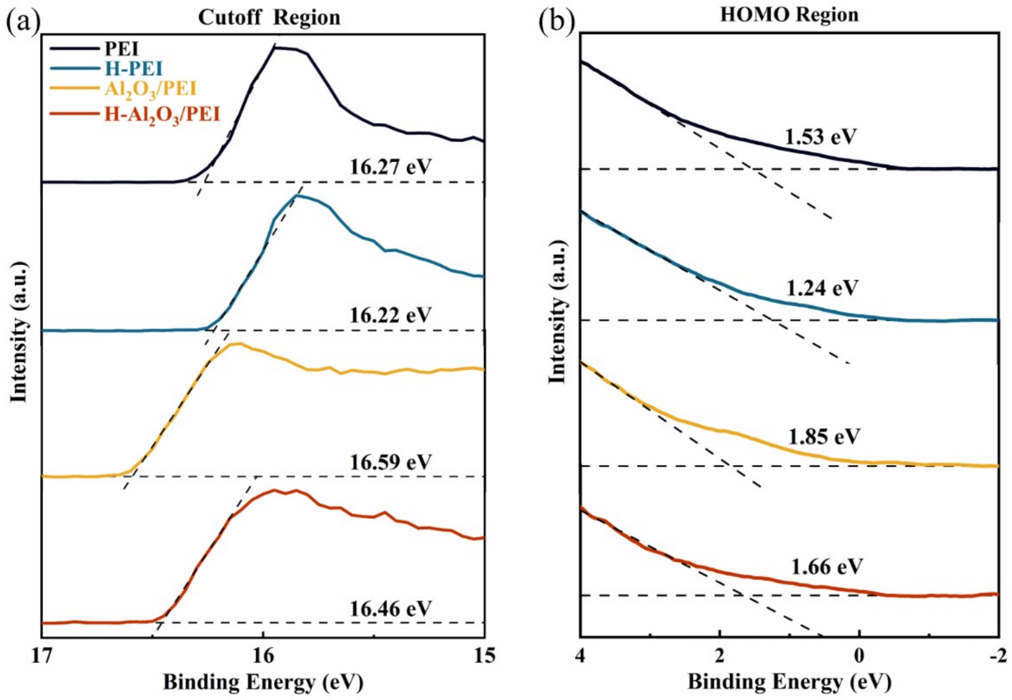

Figure S24. UPS measurement of the (a) secondary electron cutoff region and (b) HOMO region of the PEI, H-PEI, Al_2O_3/PEI and H-Al_2O_3/PEI films. The E_{cutoff} values of PEI, H-PEI, Al_2O_3/PEI and H-Al_2O_3/PEI are 16.27 eV, 16.22 eV, 16.59 eV and 16.46 eV, respectively. The E_{homo} values of PEI, H-PEI, Al_2O_3/PEI and H-Al_2O_3/PEI films are 1.53 eV, 1.24 eV, 1.85 eV and 1.66 eV, respectively. The ϕ_p, calculated by the difference between the incident photoelectron energy (21.22 eV) and E_{cutoff}, are 4.95 eV, 5.00 eV, 4.63 eV and 4.76 eV for PEI, H-PEI, Al_2O_3/PEI and H-Al_2O_3/PEI films, respectively.

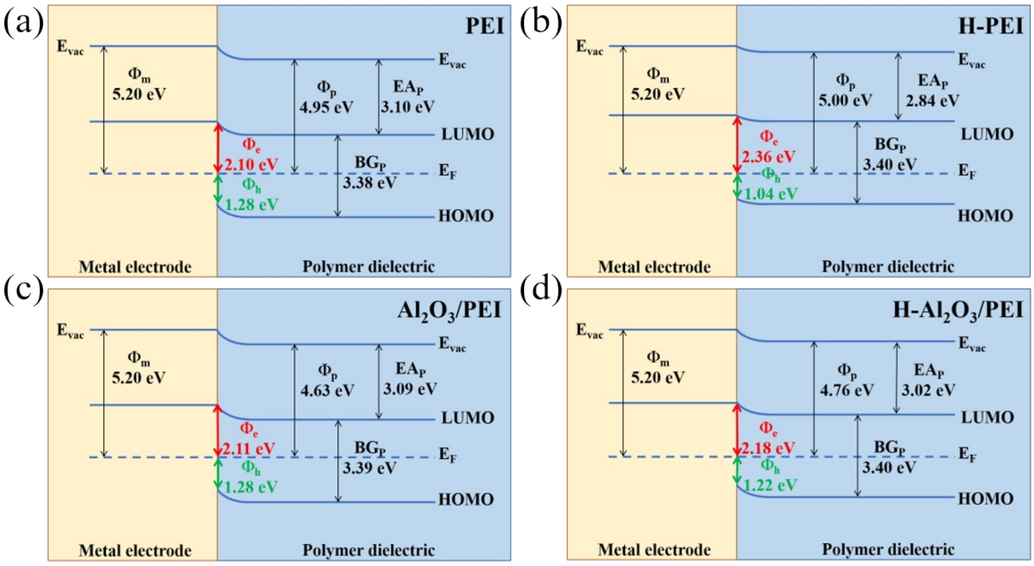

Figure S25. Band diagrams at the electrode/dielectric interface of Au/PEI, Au/H-PEI, Au/Al_2O_3/PEI and Au/H-Al_2O_3/PEI films. The work function of gold electrode (ϕ_m) (5.20 eV) is obtained from previous work.[1-2] The contact of the gold electrode and polymer dielectric will cause the alignment of their Fermi level. The ionization potential (IP) can be calculated by $IP = hv - (E_{cutoff} - E_{homo})$.[1-2] Thus, the position of HOMO level can be determined through the IP value. With the bandgap values from the UV-vis spectrum, the position of the LUMO level can be further deduced. The calculated barrier height for the electrons (ϕ_e) are 2.10 eV, 2.36 eV, 2.11 eV and 2.18 eV for PEI, H-PEI, Al_2O_3/PEI and H-Al_2O_3/PEI films, respectively. The electron affinity (EA_p) are 3.10 eV, 2.84 eV, 3.09 eV and 3.02 eV for PEI, H-PEI, Al_2O_3/PEI and H-Al_2O_3/PEI films, respectively.

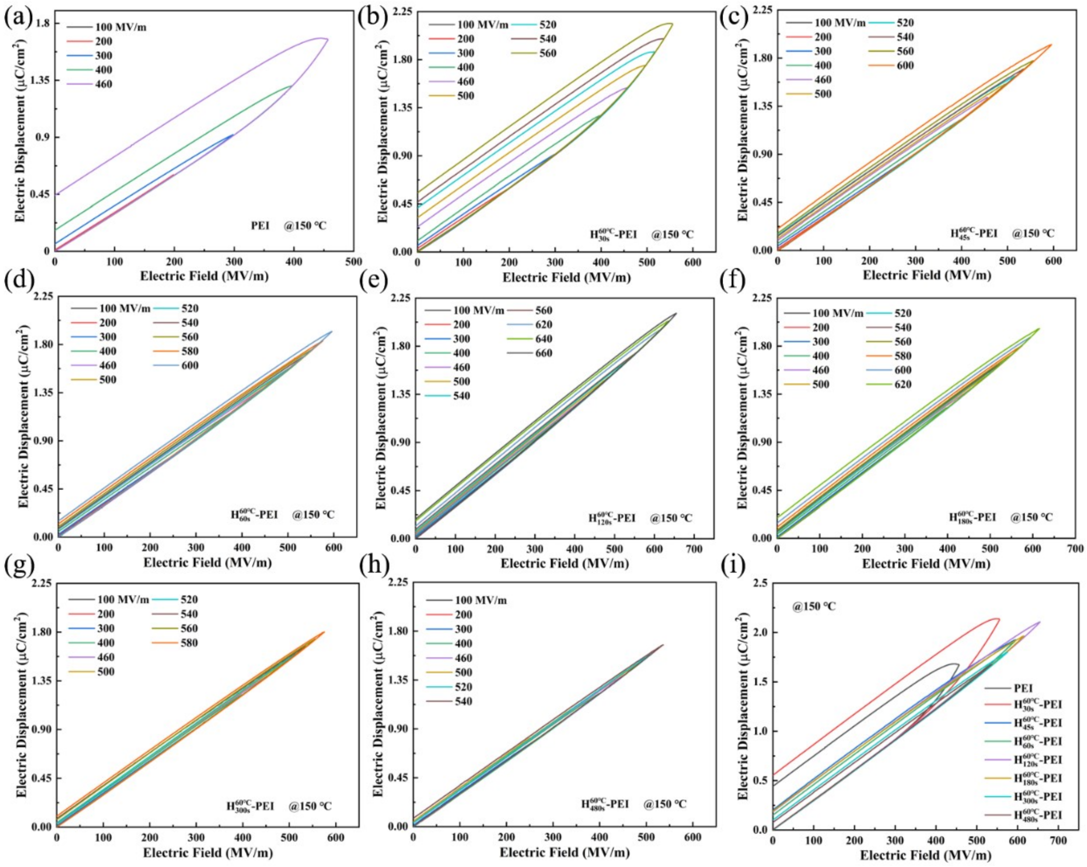

Figure S26. (a-h) Unipolar *D-E* loops of pristine PEI and H-PEI films with different hydrolysis time at 60 ℃ as a function of electric field at 150 ℃. (i) Comparison of unipolar *D-E* loops of pristine PEI and H$^{60\ ℃}$-PEI films with different hydrolysis time at 150 ℃ and $E_{b\text{-}150\ ℃}$.

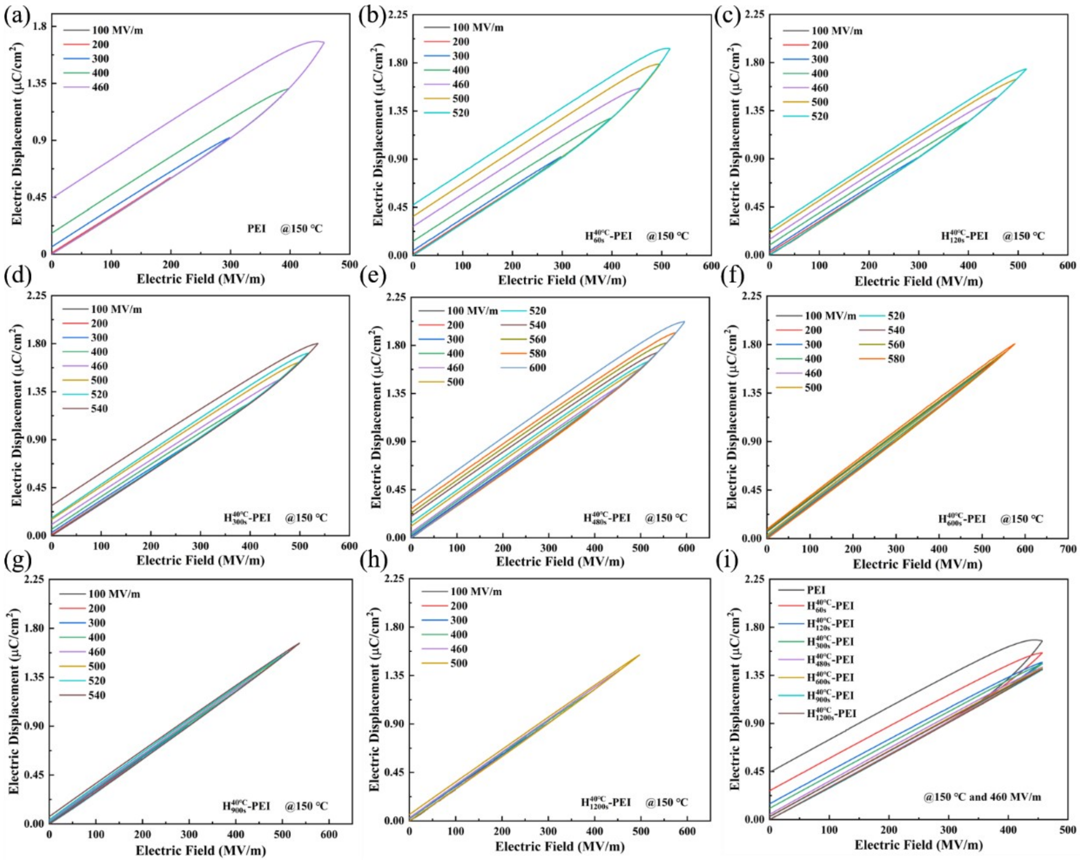

Figure S27. (a-h) Unipolar *D-E* loops of pristine PEI and H-PEI films with different hydrolysis time at 40 ℃ as a function of electric field at 150 ℃. (i) Comparison of unipolar *D-E* loops of pristine PEI and $\mathrm{H}^{40\ ℃}$-PEI films with different hydrolysis time at 150 ℃ and 460 MV/m.

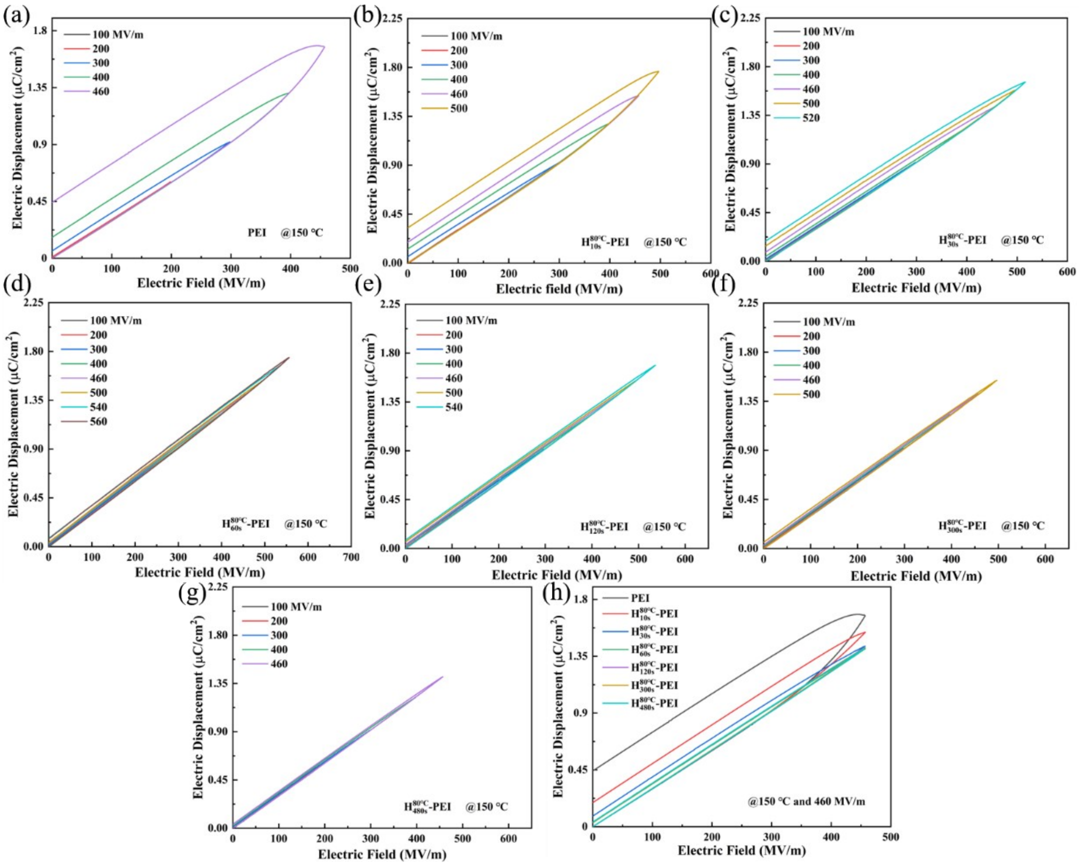

Figure S28. (a-g) Unipolar *D-E* loops of pristine PEI and H-PEI films with different hydrolysis time at 80 °C as a function of electric field at 150 °C. (h) Comparison of unipolar *D-E* loops of pristine PEI and $H^{80 ℃}$-PEI films with different hydrolysis time at 150 °C and 460 MV/m.

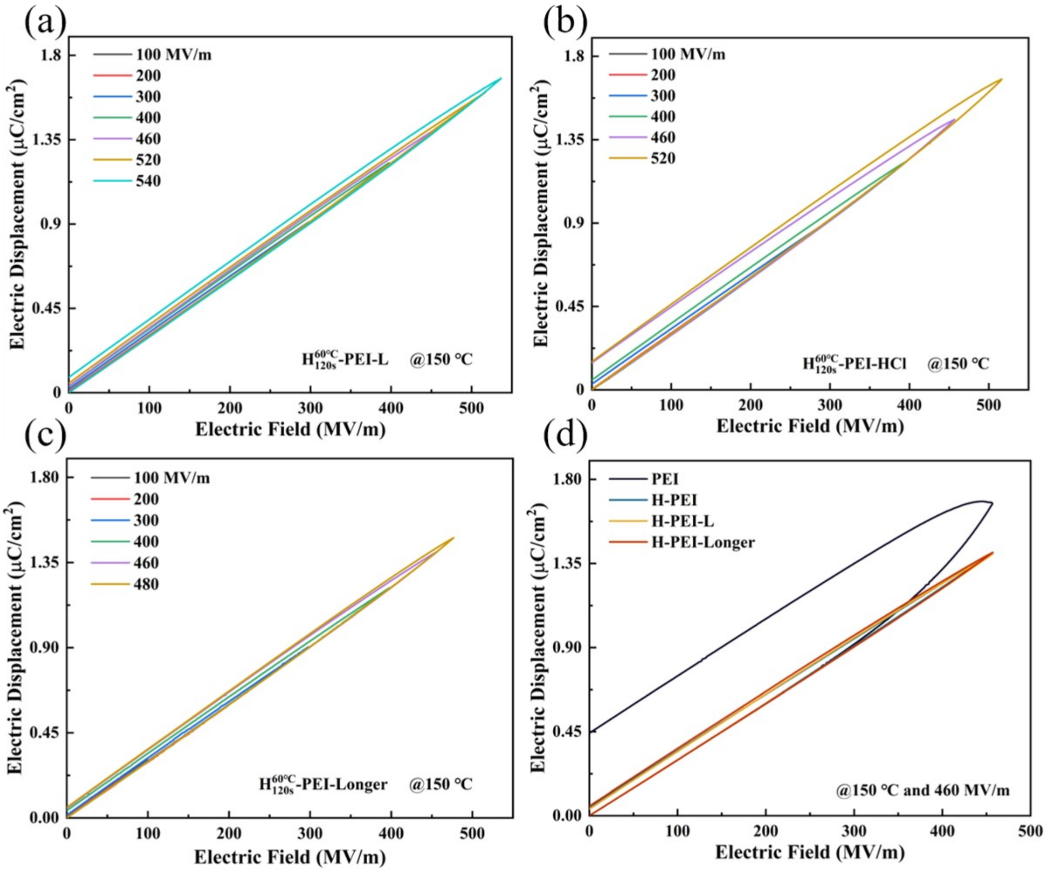

Figure S29. Unipolar *D-E* loops of (a) H-PEI-L, (b) H-PEI-HCl and (c) H-PEI-Longer films as a function of electric field at 150 °C; (d) The comparison of unipolar D-E loops of pristine PEI and hydrolyzed PEI films with different DI water rinse period at 150 °C and 460 MV/m.

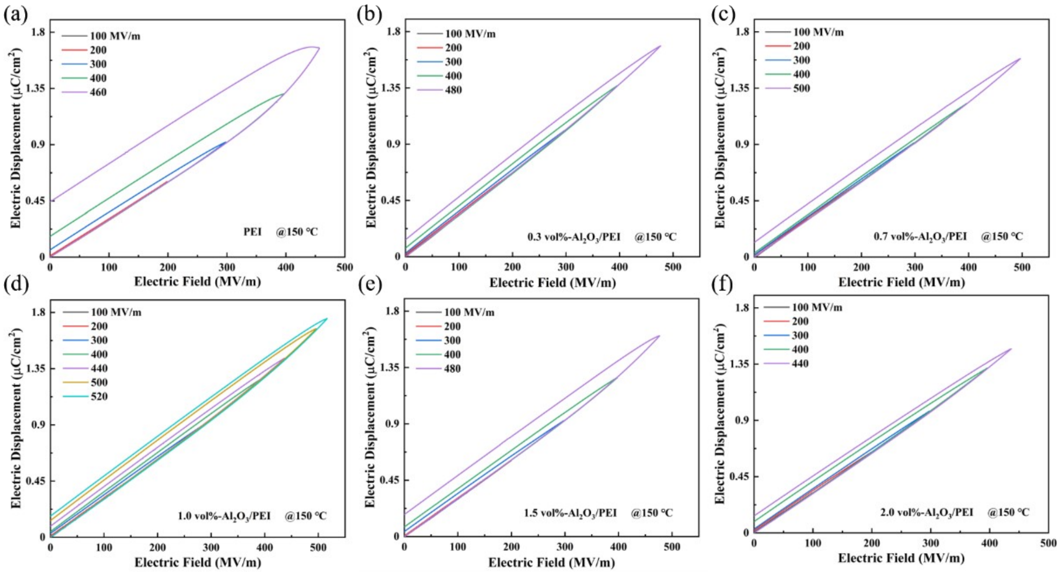

Figure S30. Unipolar *D-E* loops of (a) pristine PEI and (b-f) Al_2O_3/PEI films with different volume contents of Al_2O_3 NPs at 150 °C.

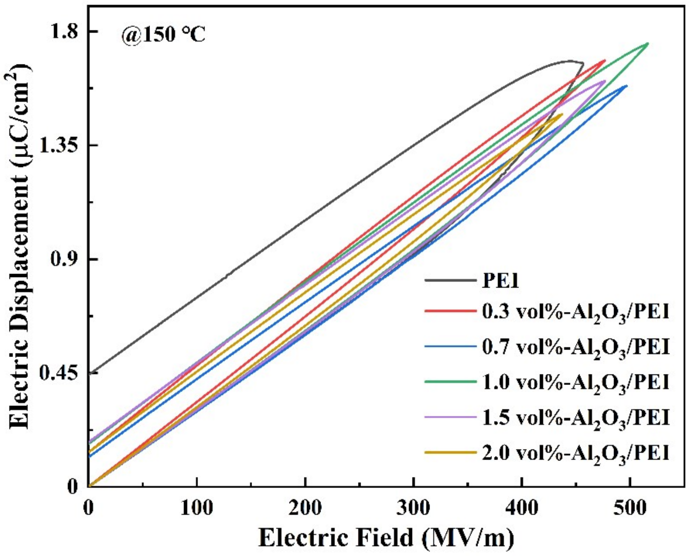

Figure S31. Comparison of unipolar *D-E* loops of pristine PEI and Al_2O_3/PEI films with different filler contents measured at 150 °C and $E_{b\text{-}150\ °C}$.

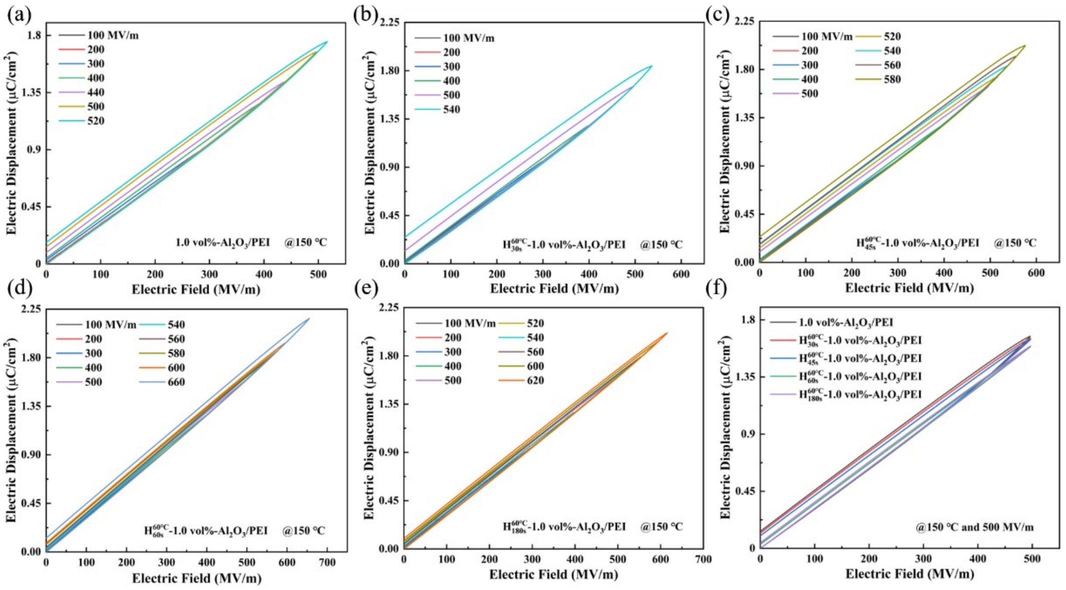

Figure S32. (a-e) Unipolar *D-E* loops of Al_2O_3/PEI and H-Al_2O_3/PEI films with different hydrolysis time as a function of electric field at 150 °C. (f) Comparison of unipolar *D-E* loops of pristine Al_2O_3/PEI and H-Al_2O_3/PEI films with different hydrolysis time at 150 °C and 500 MV/m.

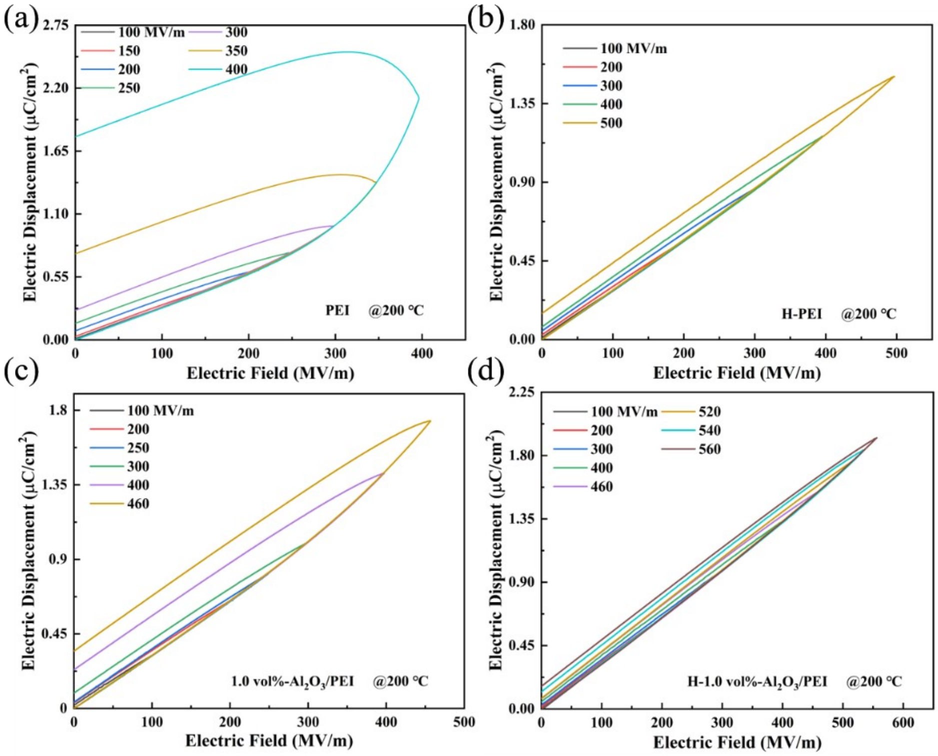

Figure S33. Unipolar *D-E* loops of (a) PEI, (b) H-PEI, (c) Al_2O_3/PEI and (d) H-Al_2O_3/PEI films as a function of electric field at 200 °C.

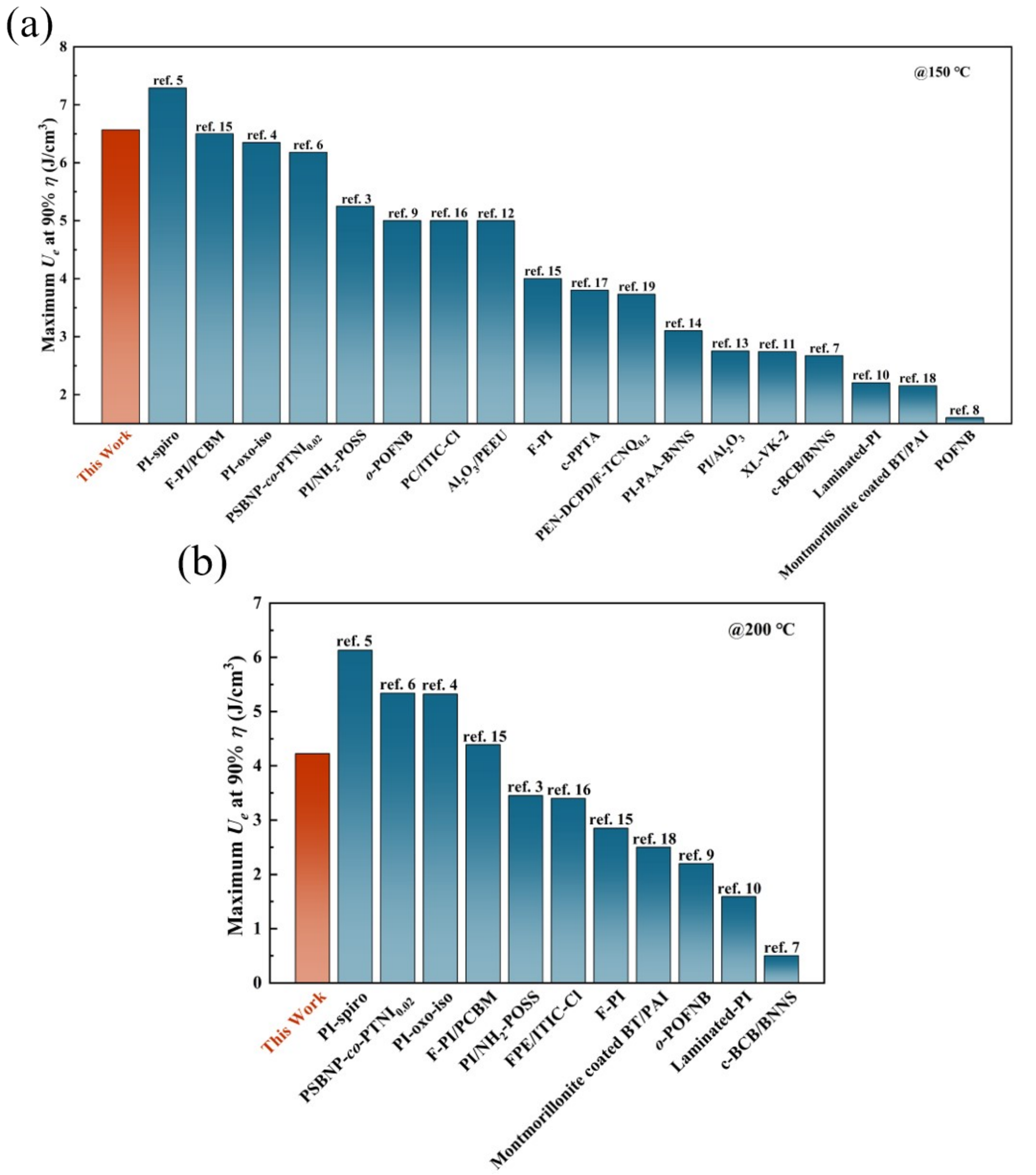

Figure S34. Comparison of the discharged energy density with an efficiency of around 90% in this work with those of previously published non PEI-based composite films at (a) 150 °C and (b) 200 °C.[3-19]

References

1. Y. Zhou, Q. Li, B. Dang, Y. Yang, T. Shao, H. Li, J. Hu, R. Zeng, J. He and Q. Wang, *Advanced Materials*, 2018, **30**, 1805672.
2. C. Yuan, Y. Zhou, Y. Zhu, J. Liang, S. Wang, S. Peng, Y. Li, S. Cheng, M. Yang, J. Hu, B. Zhang, R. Zeng, J. He and Q. Li, *Nature Communications*, 2020, **11**, 3919.
3. J. Dong, L. Li, P. Qiu, Y. Pan, Y. Niu, L. Sun, Z. Pan, Y. Liu, L. Tan and X. Xu, *Advanced Materials*, 2023, **35**, 2211487.
4. R. Wang, Y. Zhu, J. Fu, M. Yang, Z. Ran, J. Li, M. Li, J. Hu, J. He and Q. Li, *Nature*

Communications, 2023, **14**, 2406.

5. Z. Ran, R. Wang, J. Fu, M. Yang, M. Li, J. Hu, J. He and Q. Li, *Advanced Materials*, 2023, 2303849.
6. J. Chen, Y. Zhou, X. Huang, C. Yu, D. Han, A. Wang, Y. Zhu, K. Shi, Q. Kang and P. Li, *Nature*, 2023, **615**, 62-66.
7. Q. Li, L. Chen, M. R. Gadinski, S. Zhang, G. Zhang, H. U. Li, E. Iagodkine, A. Haque, L.-Q. Chen and T. N. Jackson, *Nature*, 2015, **523**, 576-579.
8. C. Wu, A. A. Deshmukh, Z. Li, L. Chen, A. Alamri, Y. Wang, R. Ramprasad, G. A. Sotzing and Y. Cao, *Advanced Materials*, 2020, **32**, 2000499.
9. A. A. Deshmukh, C. Wu, O. Yassin, A. Mishra, L. Chen, A. Alamri, Z. Li, J. Zhou, Z. Mutlu and M. Sotzing, *Energy & Environmental Science*, 2022, **15**, 1307-1314.
10. J. Dong, R. Hu, X. Xu, J. Chen, Y. Niu, F. Wang, J. Hao, K. Wu, Q. Wang and H. Wang, *Advanced Functional Materials*, 2021, **31**, 2102644.
11. H. Li, M. R. Gadinski, Y. Huang, L. Ren, Y. Zhou, D. Ai, Z. Han, B. Yao and Q. Wang, *Energy & Environmental Science*, 2020, **13**, 1279-1286.
12. T. Zhang, X. Chen, Y. Thakur, B. Lu, Q. Zhang, J. Runt and Q. Zhang, *Science advances*, 2020, **6**, eaax6622.
13. D. Ai, H. Li, Y. Zhou, L. Ren, Z. Han, B. Yao, W. Zhou, L. Zhao, J. Xu and Q. Wang, *Advanced Energy Materials*, 2020, **10**, 1903881.
14. Z. Dai, Z. Bao, S. Ding, C. Liu, H. Sun, H. Wang, X. Zhou, Y. Wang, Y. Yin and X. Li, *Advanced Materials*, 2022, **34**, 2101976.
15. W. Ren, M. Yang, L. Zhou, Y. Fan, S. He, J. Pan, T. Tang, Y. Xiao, C. W. Nan and Y. Shen, *Advanced Materials*, 2022, **34**, 2207421.
16. Y. Zhou, Y. Zhu, W. Xu and Q. Wang, *Advanced Energy Materials*, 2023, **13**, 2203961.
17. J. Yan, H. Wang, J. Zeng, X. Zhang, C. W. Nan and S. Zhang, *Small*, 2023, 2304310.
18. Y. Wang, Z. Li, T. J. Moran, L. A. Ortiz, C. Wu, A. C. Konstantinou, H. Nguyen, J. Zhou, J. Huo and K. Davis ‐ Amendola, *Advanced Science*, 2022, **9**, 2204760.
19. J. Chen, Z. Pei, Y. Liu, K. Shi, Y. Zhu, Z. Zhang, P. Jiang and X. Huang, *Advanced Materials*, 2023, **35**, 2306562.